

# Morphological Study of Directionally Freeze-Cast Nickel Foams



HYUNGYUNG JO, MIN JEONG KIM, HYELIM CHOI, YUNG-EUN SUNG, HEEMAN CHOE, and DAVID C. DUNAND

Nickel foams, consisting of 51 to 62 pct aligned, elongated pores surrounded by a network of Ni walls, were fabricated by reduction and sintering of directionally cast suspensions of nanometric NiO powders in water. Use of dispersant in the slurry considerably affected the foam morphology and microstructure at both the micro- and macro-scale, most likely by modifying ice solidification into dendrites (creating the aligned, elongated macro-pores) and NiO powder accumulation in the inter-dendritic space (creating the Ni walls with micro-pores). The mean width of the Ni walls, in foams solidified with and without dispersant, was  $21 \pm 5$  and  $75 \pm 13$   $\mu\text{m}$ , respectively. Additionally, the foams with the dispersant showed less dense walls and rougher surfaces than those without the dispersant. Moreover, the fraction of closed pores present in the foam walls with the dispersant was higher than that of the samples without dispersant. We finally verified the potential energy application of the Ni foam produced in this study by carrying out a preliminary single-cell performance test with the Ni foam sample as the gas diffusion layer on the anode side of a polymer electrolyte membrane fuel cell.

DOI: 10.1007/s40553-016-0068-y

© ASM International (ASM) and The Minerals, Metals & Materials Society (TMS) 2016

## I. INTRODUCTION

POROUS or foamed metals have recently attracted increasing interest as advanced functional materials for a wide range of engineering applications, such as battery electrodes, catalysts, heat exchangers, and filters.<sup>[1-6]</sup> In particular, since nickel inherently possesses high corrosion resistance, catalytic activity, high electrical conductivity, and high melting temperature, nickel-based foams are promising materials for energy applications, such as lithium ion batteries, dye-sensitized solar cells, and solid oxide fuel cells, as schematically illustrated in Figure 1. Open porous metallic electrodes can enable efficient and rapid electrochemical reactions because of their high specific surface area.<sup>[1]</sup>

Established processing routes for nickel foams include pulsed electrodeposition or electroless plating on substrates, powder sintering, replication casting, and chemical vapor deposition methods.<sup>[7-11]</sup> Freeze-casting, also known as ice-templating, is a promising novel technique to fabricate porous materials, as it provides easy scalability and control of the size, volume fraction,

orientation, and shape of the pores.<sup>[12]</sup> Typical freeze-casting method consists of dispersing particles in slurry which is then frozen in the regime where dendrites are formed and particles are pushed into inter-dendritic space. Sublimation under reduced pressure creates large pores where the particle-free dendrites were present surrounded by a network of walls consisting of loosely bond particles. Upon subsequent sintering the walls are densified, creating a scaffold with equiaxed pores, or, if solidification was performed in a directional manner, with aligned, elongated pores. In the past decades, the freeze-casting method has been extensively studied for the production of porous ceramics.<sup>[13]</sup> Only recently have metal foams been created by directional freeze-casting, by using metallic powders (for titanium) or oxide powders (for copper and iron) that are later reduced during the sintering step.<sup>[14-16]</sup>

In the present study, we demonstrate for the first time that nickel foams with aligned, elongated pores can be created by directional freeze-casting of nickel oxide, followed by sintering and reduction to metallic nickel. The use of nickel oxide powders, rather than metallic nickel powders, presents two advantages: first, the oxide has lower density than the metal ( $6.7$  vs  $8.9$   $\text{g}/\text{cm}^3$ ), reducing the settling in the suspension; second, much finer powders (nano-size rather than micro-size) can be used without oxidation or rapid reaction in water. The nano-sized powders are preferable to coarser, micro-sized powders for several reasons: (i) they settle in the slurry more slowly; (ii) they are more easily pushed by the ice dendrites; (iii) they sinter more easily; (iv) they are reduced more rapidly; and (v) after sintering, they create walls surfaces that have higher specific area. For nanoparticle dispersion, it is important to overcome the

HYUNGYUNG JO, Master's Student, HYELIM CHOI, Research Professor, and HEEMAN CHOE, Associate Professor, are with the School of Advanced Materials Engineering, Kookmin University, 77 Jeongneung-ro, Seongbuk-gu, Seoul 136-702, Korea. MIN JEONG KIM, Ph.D. Student, and YUNG-EUN SUNG, Professor, are with the Center for Nanoparticle Research, Institute for Basic Science (IBS), Seoul 151-742, Korea, and also with the School of Chemical and Biological Engineering, Seoul National University, Seoul 151-742, Korea. DAVID C. DUNAND, Professor, is with the Department of Materials Science and Engineering, Northwestern University, Evanston, IL 60208. Contact e-mail: dunand@northwestern.edu

Manuscript submitted August 17, 2015.

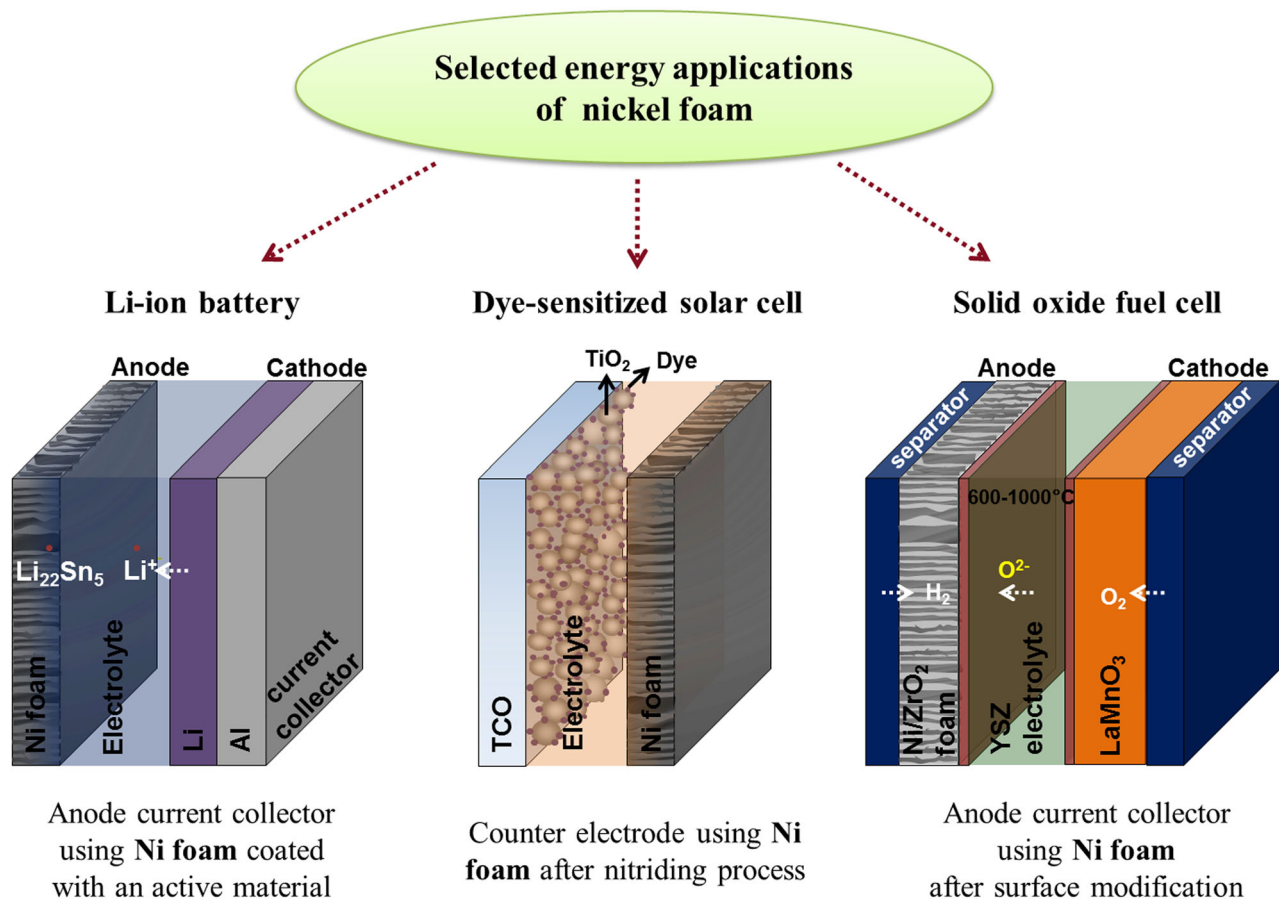


Fig. 1—Schematic illustration of the potential applications in energy devices of directional Ni foams fabricated in this study.

associated significant total surface energy. It was found that when nanoparticles are dispersed in liquid, their hydrodynamic size is often larger than the primary particle size.<sup>[17]</sup> The stability of nanoparticle dispersion and its tendency toward agglomeration can be considered in the context of electrostatic, steric, and van der Waals forces between particles using the Derjaguin–Landau–Verwey–Overbeek (DLVO) theory.<sup>[18]</sup> In particular, this study focuses on the effect of the dispersant and demonstrates its importance in achieving good suspension conditions by observing the microstructure and analyzing the porosity of the sintered, reduced foams.

## II. EXPERIMENTAL PROCEDURES

Commercially available nickel oxide powder (NiO) with an average particle size <20 nm (Inframat Advanced Materials, USA) was used. Polyvinyl alcohol (PVA) with a molecular weight in the range from 89,000 to 98,000 g mol<sup>-1</sup> (Sigma-Aldrich, USA) was used as a binder. The slurry was prepared according to the following consecutive steps. A mixture of 11 wt pct PVA binder in 20 mL of deionized (DI) water was initially degassed under vacuum. The mixture was then boiled to dissolve the binder and subsequently allowed

to cool down. NiO powder (5 g) was then poured and mixed in the water/binder solution. To improve the stability of the suspension, 0.09 g of Darvan 811 (a low-molecular-weight sodium polyacrylate powder dispersant from R.T. Vanderbilt Co., USA) was added as a dispersant. The slurry was dispersed by using mechanical stirring and sonication for 1 hour to break down the large oxide powder agglomerates, and then cooled down to a few degrees above the freezing point of water.

The cold slurry was then poured into a 36-mm inner-diameter polytetrafluoroethylene (PTFE) mold placed on the top of a copper rod to achieve directional solidification at a fixed copper temperature of 263 K (−10 °C). The entire side of the mold was insulated with polystyrene foam and the other end of the copper rod was placed in a steel container filled with liquid nitrogen along with ethyl alcohol (to control the ice-cooling rate). Once complete solidification was achieved (after ~60 minutes), the frozen sample, approximately 90 mm in height, was removed from the mold and sublimated at 185 K (−88 °C) for 48 hours in a freeze-dryer under 0.005 torr residual atmosphere. The resulting green body was transferred to a furnace, heated to 573 K (300 °C), and then maintained at that temperature for 2 hours to remove the binder and reduce the oxide, and then sintered at 1273 K (1000 °C) under an Ar-5 pct H<sub>2</sub>

gas mixture. Heating rates were 296 K/min (23 °C/min) and the final cooling rate was 275 K/min (2 °C/min).

To perform the microstructural analysis, the final sintered sample was mounted in epoxy and polished after being cut into pieces with a diamond saw both in parallel and perpendicular directions with respect to the direction of the pore growth. The microstructure of the Ni foam was imaged by optical and scanning electron microscopy (SEM, JSM7401F, JEOL). X-ray diffraction (XRD, Rigaku Ultima III X-ray diffractometer) was also used to determine and compare the phases before and after the reduction process. Additionally, mercury intrusion porosimetry (MIP, AutoPore IV Micromeritics, Micromeritics, USA) was used to characterize the pore size and distribution of the Ni foams.

To investigate the performance of the foams as a polymer electrolyte membrane fuel cell (PEMFC) electrode, a Nafion<sup>®</sup> 212 membrane (DuPont) was used for the ion-conducting membrane, which was immersed in a 2.5 pct H<sub>2</sub>O<sub>2</sub> solution at 353 K (80 °C) for 1 hour and then rinsed in boiling DI water for 1 hour for purification. The membrane was then boiled again in a 0.5 M H<sub>2</sub>SO<sub>4</sub> solution for 1 hour and rinsed in DI water for protonation. The 40 wt pct Pt/C (Johnson Matthey Co.) catalyst was dispersed in a mixture of isopropyl alcohol, DI water, and perfluorosulfonic acid ionomer (5 wt pct Nafion<sup>®</sup> ionomer, Aldrich) to prepare the catalyst ink. A spraying method was used to form the Pt catalyst layer with a Pt loading of 0.2 mg/cm<sup>2</sup> on the Nafion<sup>®</sup> 212 membrane (an area of 1 cm<sup>2</sup>). With carbon paper containing microporous layers (35BC, SGL) used as cathode gas diffusion layer (GDL), two set-ups—our Ni foam and a commercial GDL (Toray 060, Toray, Japan)—were tested and compared as the anode GDL. The membrane electrode assemblies (MEAs) were inserted into a single-cell unit of PEMFC that had a graphite plate with a serpentine gas flow channel. A single-cell unit was assembled with eight screws and tightening torque of 7.5 Nm. Polarization curves were obtained with the current-sweep method using a fuel-cell test system. The tests were carried out at 353 K (80 °C) with fully humidified H<sub>2</sub>/O<sub>2</sub> gases fed into the anode and cathode inlets, respectively, with an anode stoichiometry of 2 and a cathode stoichiometry of 9.5.

### III. RESULTS AND DISCUSSION

During the first heat-treatment process, the NiO particles were expected to be reduced at around 573 K (300 °C) with PVA binder eliminated.<sup>[19]</sup> NiO reduction temperatures can vary from 423 K to 873 K (150 °C to 600 °C), depending on the experimental conditions and the morphology of the oxide particles.<sup>[20–23]</sup> During this process, H<sub>2</sub> adsorbs and dissociates on two Ni atoms that are located adjacent to an oxygen vacancy leading to the nucleation and growth of Ni clusters. These Ni domains autocatalytically grow by the movement of interfaces of (NiO/Ni) with pores forming within larger particles. Subsequently, smaller particles shrink to accommodate the Ni densification and volume loss.<sup>[24]</sup> The sintering step [1273 K (1000 °C)] of the reduced Ni

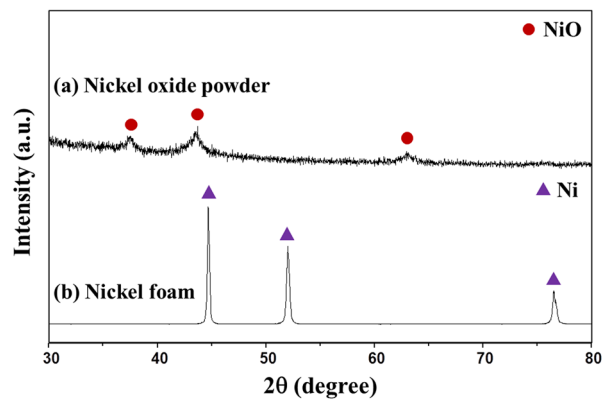


Fig. 2—XRD patterns of (a) the NiO precursor powder and (b) freeze-cast Ni foam with dispersant after reduction and sintering steps.

powders resulted in continuous, mostly densified Ni walls surrounding aligned elongated plate-like pores, as reported previously for freeze-cast and sintered Ti and Cu foams.<sup>[14,15]</sup> After sintering, the initial sample volume of the NiO foam decreased by  $83 \pm 0.5$  pct (from the green body to pure Ni foam), which was caused by both removal of oxygen and sintering densification. The XRD pattern, shown in Figure 2, confirms that the Ni foam was fully reduced and contained no measurable NiO powder.

Figure 3(a) shows the microstructure of the Ni foam created with dispersant in a longitudinal direction where the typical lamellar structure can be observed entirely from the bottom through the top of a shorter sample with a height of 1.3 mm, much less than the normal height of ~90 mm. The walls are almost parallel to each other and fairly well aligned along the direction of freezing, which is vertical in Figure 3(a). Because the slurry was poured on the cold Cu finger maintained at a constant temperature of 253 K (−20 °C) during the freezing stage, the ice nucleation occurred under a state of high supercooling, and the bottom region thus exhibits relatively thinner longitudinal pores and dendrites with a smaller wall width resulting from a faster freezing kinetics.<sup>[25]</sup> However, the freezing kinetics slowed down as the dendrite grew and hence, thicker longitudinal pores and dendrites with larger walls were formed.

Two competing growth tendencies of the ice crystals must be considered when interpreting the dendrite growth morphology of the foam processed *via* freeze-casting: the growth tendency in the direction parallel to the macroscopic temperature gradient and the ‘preferred’ growth tendency in the direction toward the lowest energy interface.<sup>[26]</sup> The competition between these two growth tendencies causes two characteristic phenomena: the formation of secondary dendrites on the lamellar ice crystals and the tilted orientation growth of the crystals growing at a fast cooling rate with respect to the temperature gradient, as shown in Figures 3(a) and (b).<sup>[27]</sup>

Figure 4 shows the transverse (radial) and longitudinal views at the center of a cross-section of the Ni foam created with dispersant, shown at low and high

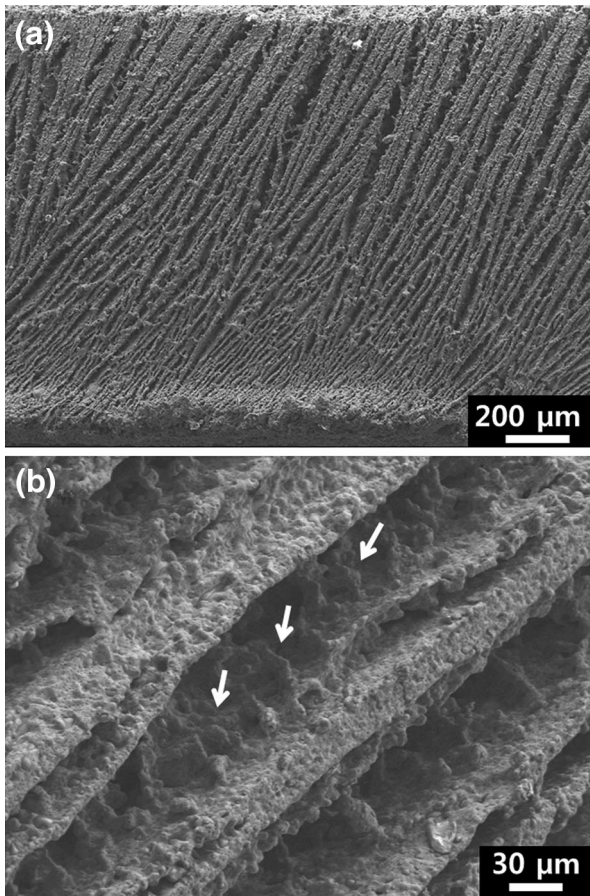


Fig. 3—SEM images of a freeze-cast, reduced, and sintered Ni foam with dispersant (total height of 1.3 mm): (a) typical morphology of lamellar macro-pores created by the ice template grown during freezing and (b) secondary dendrites on the Ni walls.

magnifications for comparison. The black areas in the optical micrographs in Figure 4 correspond to the epoxy resin used to fill the pores during metallographic mounting. In the transverse cross-sectional views of Figures 4(a) through (c), dendritic walls appear to be locally directional (Figure 4(c)), but with all orientations visible at a larger scale (Figure 4(a)). Notably, the morphology of the Ni foam is determined not only by the nucleation conditions, but also by the solidification kinetics.<sup>[28]</sup> After the randomly oriented rapid growth of the ice crystals near the contact point with the cold finger, a single solidification front consisting of numerous grains appears and grows in the direction of the temperature gradient, which then leads to an oriented and continuous lamellar dendrite architecture in both parallel and perpendicular directions to the ice front. In the longitudinal cross-sectional view of Figures 4(d) through (f), the individual walls are shown from which the mean widths of the plate-like elongated pores and walls are measured as  $69 \pm 19$  and  $70 \pm 12$   $\mu\text{m}$ , respectively. Additionally, much smaller pores on the surface of the walls, some of which are highlighted in Figure 4(f), are assumed to result from an incomplete sintering process. Closed micro-pores are also visible within the walls.

Figure 5 shows SEM micrographs of the top (Figure 5(a)) and fractured side (Figure 5(b)) of an inner wall of a Ni foam specimen created with dispersant. The high roughness observed for the entire sample surface resulted from the incomplete sintering process that led to the formation of the smaller micro-pores shown by both optical microscopy and SEM. This structure is advantageous with respect to providing a high specific surface area for use as an electrode in energy applications. However, reductions in wall stiffness, strength, and ductility can also be anticipated and should be considered if the Ni foam is to be used for structural applications.

Figure 6 compares SEM micrographs of fractured surfaces of Ni foams with and without dispersant in the slurry. No noticeable difference in morphology is observed when comparing the side views of vertical cross-section of the two Ni foams, as shown in Figure 6. Conversely, a considerable difference in morphology is observed when comparing the top views of the cross-section of the two samples perpendicular to the growth direction, as shown more systematically in Figure 7, which shows the natural top surface of the samples. In comparison to the Ni foam with dispersant (Figure 7(d)), the Ni foam without dispersant (Figure 7(a)) shows thicker Ni walls. Neighboring elongated pores in Ni foam with dispersant are orientated in a fairly parallel direction, into colonies with width and length on the order of hundreds of micrometers. The heterogeneous nucleation of ice is still dominant and the anisotropic growth occurs, because the hexagonal ice crystals grow generally along a preferred growth direction mostly aligned to the solidification direction.<sup>[29]</sup> The mean width values of the Ni foam walls with and without dispersant are measured as  $21 \pm 5$  and  $75 \pm 1$   $\mu\text{m}$ , respectively. Thus, within a colony, a larger number of thinner ice dendrites (and thus inter-dendritic regions forming Ni walls after sintering) were formed in the slurry containing the dispersant, as shown in Figures 7(d) and (e). In addition, the presence of dispersant in the slurry hinders the particles from agglomerating, and hence, less dense walls with rougher surface are obtained by affecting the particle-particle interactions.<sup>[30,31]</sup> Comparison of Figures 7(c) and (f) indeed shows that the Ni foams with dispersant exhibit less dense walls with rougher surface than those without dispersant.

The addition of dispersant can reduce viscosity and lower the freezing temperature of a slurry, and hence, substantially affects the pore and wall morphology by modifying both the physical properties of the slurry and its ice dendritic solidification kinetics.<sup>[30]</sup> Here, we briefly describe changes in the physical properties of slurry and its ice dendritic solidification kinetics based on the previously reported mechanism, and also attempt to explain the salient mechanism associated with the differences in morphology between the Ni foams without and with dispersant.

First, change in the physical properties of slurry through the addition of dispersant can modify the sedimentation behavior and viscosity of the slurry.<sup>[31]</sup> In general, particles in slurry can be dispersed by an

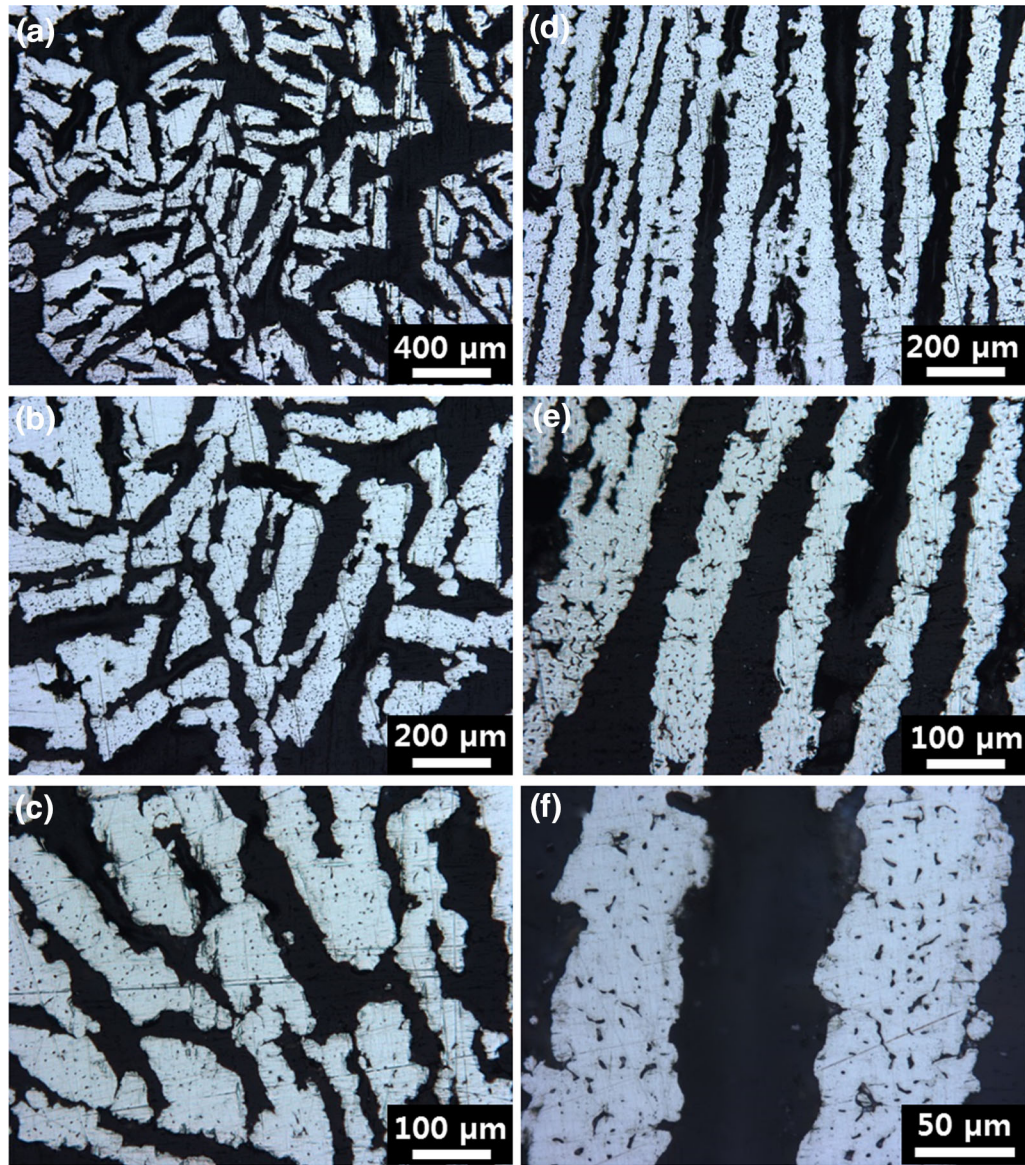


Fig. 4—Optical micrographs of a mounted and polished Ni foam (with dispersant) cross-section cut (*a, b, c*) perpendicular and (*d, e, f*) parallel to the freezing direction.

electrostatic, steric, or electro-steric stabilization mechanism.<sup>[32]</sup> Sodium polyacrylate in Darvan 811 used in this study can act as an effective dispersant medium for ceramic powder slurry to prevent sedimentation, which disintegrates the particle aggregates.<sup>[33]</sup> With the addition of dispersant, the viscosity of slurry decreases because the double electric layer characteristic of Darvan 811 makes the dissociation degree as a result of a higher surface-charge density.<sup>[34]</sup> This phenomenon can be confirmed by an increase in the absolute value of zeta potential (stability degree in colloidal solution) that is controlled by the magnitude of repulsion and attraction forces between charged particles.<sup>[34]</sup>

Second, solidification kinetics is affected by the change in the physical properties of slurry through the addition of dispersant. At the beginning of solidification, the solid-liquid interface is planar. It then suffers

transition into an irregular morphology: cellular, lamellar, and finally more complex dendritic morphology.<sup>[28]</sup> The initial instability state of this transition is described by the Mullins-Sekerka instability phenomenon, which is the thermodynamic instability of the interface.<sup>[35]</sup> The wavelength distance of the interface instability decreases with increasing capillary effect between the well-dispersed fine particles, which is evidenced by the shorter lamellar distance observed for the Ni foam with dispersant than that for the Ni foam without dispersant. Additionally, ice crystal growth during solidification determines whether a particle in the slurry is rejected or trapped by the approaching liquid-solid interface. By controlling particle interaction and surface energy through the addition of dispersant, a better suspension can be achieved, eventually resulting in the formation of less dense walls with finer pores, as evidenced in Figures 7(d) through (f). Furthermore, the slurry

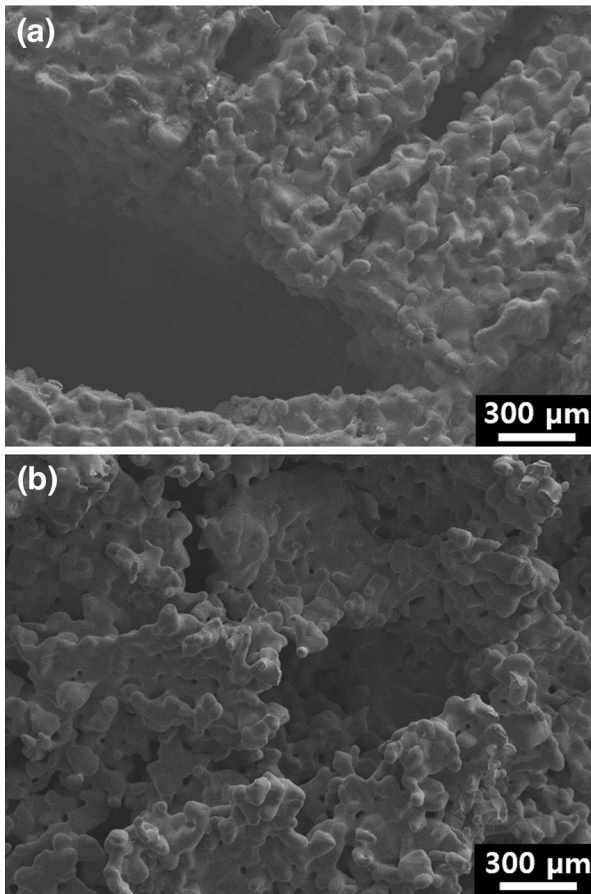


Fig. 5—SEM images of freeze-cast Ni foam with dispersant: (a) outer surface and (b) fracture surface.

without dispersant has higher viscosity than the slurry with dispersant, suggesting a longer delay for the structural reorganization of the slurry without dispersant than with dispersant.<sup>[34]</sup> The particles are thus more closely packed for the slurry without dispersant, resulting in stronger particle-particle interaction and denser walls.

The pore thickness distribution of the Ni foams with and without dispersant, determined *via* MIP is compared in Figure 8. Given the bimodal size distribution in the foams, a pressure range of 0–7 Pa was selected to detect both the smaller micro-pores and larger macro-pores. As confirmed in Figure 8, the Ni foams with and without dispersant appear to have a similar pore size distribution. They both have a bimodal pore size distribution including macro-pores formed by the presence of the ice dendrite template and micro-pores formed on the surface of a wall. However, the differences in the pore fraction and mean pore size between the Ni foams with and without dispersant are sizeable, as summarized in Table I. The porosities of the Ni foam samples with and without dispersant is 62.1 and 51.2 pct, and the mean pore diameters of the Ni foam samples with and without dispersant, determined from the MIP analysis, are 14.2 and 10.9  $\mu\text{m}$ , respectively. In Table I, the bulk and apparent densities of the Ni foams with the dispersant are 3.4 and 7.6  $\text{g}/\text{cm}^3$ , respectively, while the samples without the dispersant show 4.3 and

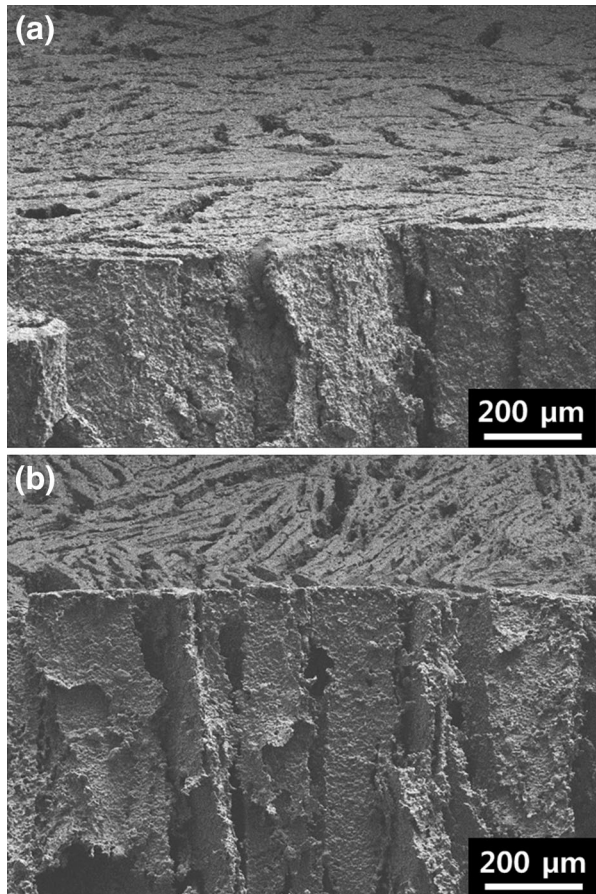


Fig. 6—SEM images of freeze-cast Ni foams cut parallel to the freezing direction: (a) Ni foam without dispersant and (b) Ni foam with dispersant.

8.0  $\text{g}/\text{cm}^3$ , respectively. Here, the apparent density indicates the density measured under a lower pressure of  $0.78 \times 10^{-10}$  MPa and is regarded as the actual density of pure Ni (8.9  $\text{g}/\text{cm}^3$ )<sup>[36]</sup> with no closed pores present in the walls. To take into account the presence of small ‘closed’ pores formed inside the walls, the apparent density was divided by the theoretical density of Ni. The calculated porosity of the closed pores for the Ni foams with and without dispersant is thus estimated to be 15 and 10 pct, respectively, indicating that the effect of the dispersant on the formation of closed pores is also substantial. Therefore, the dispersant has a strong effect on the directional freezing of NiO slurries, and thus the morphology of the resulting reduced and sintered Ni foam. This effect may be due to changes in inter-particle distance (in the slurry), water viscosity, and suspension freezing temperature.

The mechanical integrity of the freeze-cast Ni foam manufactured in this study is expected to be sufficiently high for their use as electrodes in energy application, based on a XRD analysis carried out on the inside center of the sample that was broken in pieces showing that the reduction process was complete throughout the thickness of the sample. Indeed, the Ni foams made in this study could be slightly bent, showing some degree of ductility. However, the mechanical integrity of Ni foams

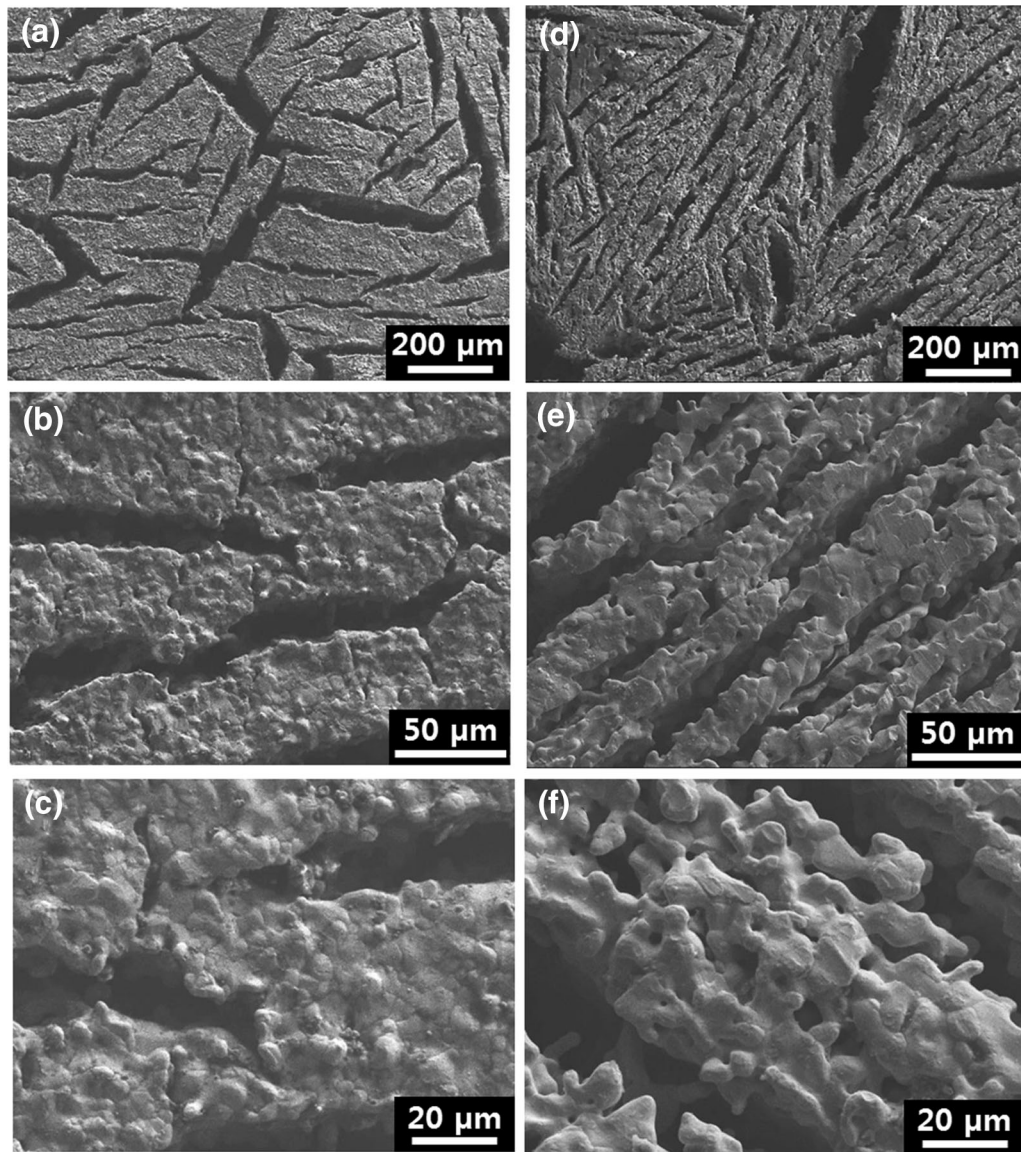


Fig. 7—SEM images of freeze-cast Ni foams' natural top surface perpendicular to the freezing direction (*a, b, c*) without and (*d, e, f*) with dispersant.

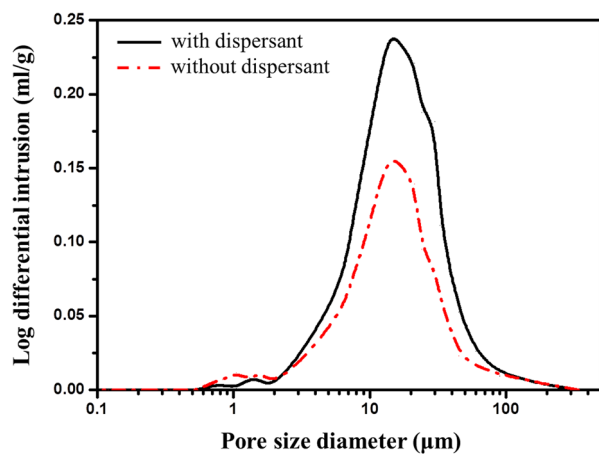


Fig. 8—Plots of the mean pore size distribution for freeze-cast Ni foams with and without dispersant.

can be improved by modifying the pore structure from elongated and aligned to equiaxed pores as previously reported.<sup>[37]</sup> A distribution of smaller, equiaxed pore structure can be achieved by freezing the oxide slurry non-directionally, but these architectures will show lower permeability than our foams with elongated pores.

Finally, to verify the potential application of the freeze-cast Ni foam for fuel cells, we carried out a performance test with the Ni foam sample as the GDL on the anode side of a PEMFC. The performance of the Ni foam anode GDL was compared with that of a commercial anode GDL. The single-cell performance test was evaluated and compared between the two MEAs containing the two GDLs attached to the catalyst-coated membrane. As shown in Figure 9, the MEA with Ni foam anode GDL shows a performance result with a maximum power density of  $421 \text{ mW/cm}^2$  at  $353 \text{ K}$  ( $80 \text{ }^\circ\text{C}$ ), which is approximately 120 pct higher

**Table I. Microstructural Parameters of Ni Foams With and Without Dispersant**

	With Dispersant	Without Dispersant
Mean pore width ( $\mu\text{m}$ )	14.2	10.9
Bulk density ( $\text{g}/\text{cm}^3$ )	3.4	4.3
Apparent density ( $\text{g}/\text{cm}^3$ )	7.6	8.0
'Closed' porosity in wall (pct)	14.6	10.1
Total porosity (pct)	62.1	51.2

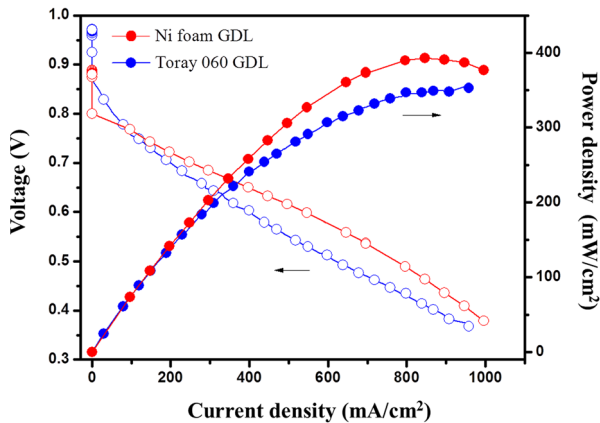


Fig. 9—Comparison of single-cell polarization curves and power density of the MEAs with the Ni foam with dispersant (initially produced with a height of 1.3 mm that was later polished down to 0.5 mm) and conventional anode GDL with a Pt loading of 0.2 mg/cm<sup>2</sup>.

than that of the MEA with the commercial anode GDL with a maximum power density of 355 mW/cm<sup>2</sup>. The improved performance of the MEA with Ni foam is most likely attributed to the lower ohmic resistance of the Ni foam relative to that of the commercial carbon-based Toray 060 GDL, because metallic material has a competitive advantage with its inherently high electrical conductivity.<sup>[37]</sup> The room-temperature electrical resistivity of bulk Ni is  $6.2 \times 10^{-6} \Omega \text{ cm}$ .<sup>[36]</sup> Given that the electrical conductivity of an open-cell metal foam and its relative density shows a near linear relationship,<sup>[38]</sup> one can estimate a room-temperature resistivity of the Ni foam (~62 pct porosity) used in this study to be approximately  $\sim 4 \times 10^{-5} \Omega \text{ cm}$ , which is considerably lower than that of Toray 060 GDL ( $\sim 8.0 \times 10^{-2} \Omega \text{ cm}$ , provided by Toray). This inherently excellent electrical conductivity of Ni foam with three-dimensionally interconnected struts results in effective electron paths with less resistance. Furthermore, it can also result in lower electrochemical impedance under H<sub>2</sub>/air supplementations and hence, decreased activation loss and lower charge-transfer compared to those of the carbon-based Toray 060 GDL.<sup>[37]</sup>

The application of the freeze-cast Ni foam to the MEA of a PEMFC as an anode GDL appears to be a success, on the basis of this single-cell performance test result. However, the long-term reliability with the Ni foam anode GDL in the PEMFC may be a potential problem to

the practical application success of the Ni foam anode GDL, because Ni is generally weak and degraded in the sulfuric acid environment, whereas highly corrosion-resistant metals such as Ti can survive well in the sulfuric environment.<sup>[37,39]</sup> Indeed, a preliminary corrosion test we carried out revealed that the Ni foam corroded and dissolved completely in a weak sulfuric acid solution of H<sub>2</sub>SO<sub>4</sub> at 343 K (70 °C) in less than 48 hours. A possible solution to this issue might be to use a Ni-based alloy with a stronger corrosion resistance such as Ni-Cu alloy for the sulfuric environment of the PEMFC.<sup>[39]</sup> Mixed NiO and CuO can then be freeze-cast, co-reduced, and inter-diffused to form the final alloy in the same process described here for pure NiO.

#### IV. CONCLUSIONS

Nickel foams with oriented elongated plate-like pores surrounded by nickel walls were fabricated by using a freeze-casting method where NiO powder aqueous slurry was directionally frozen, freeze-dried, hydrogen-reduced, and sintered. The morphology and microstructure of the pores created from solidification of slurries with and without addition of a dispersant were found to vary considerably. The Ni foams created from slurries with a dispersant showed less dense walls, rougher wall surfaces, and narrower wall width than those without the dispersant. The overall porosities were 61 and 52 pct, respectively. In addition, to demonstrate the application of these directional Ni foams to a fuel cell, a single-cell performance test was carried out with the Ni foam as the GDL on the anode side of the PEMFC and was compared with that of a commercial anode GDL. The MEA with Ni foam anode GDL shows a 27 pct higher performance than the MEA with a Toray 060 anode GDL at 0.6 V.

#### ACKNOWLEDGMENTS

This study was supported by the Priority (2012-0006680) and Pioneer (2011-0001684) Research Centers Programs through NRF. HC also acknowledges supports from the International Research and Development Program (NRF-2013K1A3A1A39074064) and the Basic Science Research Program (2014R1A2A1A11052 513). DCD also acknowledges support from the Institute for Sustainability and Energy at Northwestern University (ISEN). YS acknowledges the Institute for Basic Science (IBS) in Korea by the Project Code (IBS-R006-G1).

#### REFERENCES

1. H.C. Shin and M. Liu: *Adv. Funct. Mater.*, 2005, vol. 15, pp. 582–86.
2. L. Giani, G. Groppi, and E. Tronconi: *Ind. Eng. Chem. Res.*, 2005, vol. 44, pp. 4993–5002.
3. K.C. Leong and L.W. Jin: *Int. J. Heat Fluid Flow*, 2006, vol. 27, pp. 144–53.

4. J. Adler: *Int. J. Appl. Ceram. Technol.*, 2005, vol. 2, pp. 429–39.
5. L. Lefebvre, J. Banhart, and D.C. Dunand: *Adv. Eng. Mater.*, 2008, vol. 28, pp. 769–74.
6. P. Colombo, D.C. Dunand, and V. Kumar: *J. Mater. Res.*, 2013, vol. 28, pp. 2187–90.
7. V. Ganesh, V. Lakshminarayanan, and S. Pitchumani: *Electrochem. Solid State Lett.*, 2005, vol. 8, pp. A308–12.
8. H. Park, C. Ahn, H. Jo, M. Choi, D.S. Kim, D.K. Kim, S. Jeon, and H. Choe: *Mater. Lett.*, 2014, vol. 129, pp. 174–77.
9. M. Gauthier, L.-P. Lefebvre, Y. Thomas, and M.N. Bureau: *Mater. Manuf. Process.*, 2004, vol. 19, pp. 793–811.
10. V. Paserin, S. Marcuson, J. Shu, and D.S. Wilkinson: *Adv. Eng. Mater.*, 2004, vol. 6, pp. 454–59.
11. Y. Boonyongmaneerat and D.C. Dunand: *Adv. Eng. Mater.*, 2008, vol. 10, pp. 379–83.
12. S. Deville: *Materials*, 2010, vol. 3, pp. 1913–27.
13. E. Munch, J. Franco, S. Deville, P. Hunger, E. Saiz, and A.P. Tomsia: *JOM*, 2008, vol. 60, pp. 54–58.
14. J.L. Fife, J.C. Li, D.C. Dunand, and P.W. Voorhees: *J. Mater. Res.*, 2009, vol. 24, pp. 117–24.
15. A.I.C. Ramos and D.C. Dunand: *Metals*, 2012, vol. 2, pp. 265–73.
16. R. Sepulveda, A.A. Plunk, and D.C. Dunand: *Mater. Lett.*, 2015, vol. 142, pp. 56–59.
17. J. Jiang, G. Oberdorster, and P. Biswas: *J. Nanopart. Res.*, 2009, vol. 11, pp. 77–89.
18. M.J. Rosen and J.T. Kunjappu: *Surfactants and Interfacial Phenomena*, 4th ed., Wiley, New Jersey, US, 2012.
19. B. Jankovic, B. Adnadic, and S. Mentus: *Chem. Eng. Sci.*, 2008, vol. 63, pp. 567–75.
20. G. Parravano: *J. Am. Chem. Soc.*, 1952, vol. 74, pp. 1194–98.
21. J.A. Rodriguez, J.C. Hanson, A.I. Frenkel, J.Y. Kim, and M. Perez: *J. Am. Chem. Soc.*, 2002, vol. 124, pp. 346–54.
22. J.T. Richardson, R. Scates, and M.V. Twigg: *Appl. Catal. A*, 2003, vol. 246, pp. 137–50.
23. T.A. Utigard, M. Wu, G. Plascencia, and T. Marin: *Chem. Eng. Sci.*, 2005, vol. 60, pp. 2061–68.
24. Q. Jeangros, T.W. Hansen, J.B. Wagner, C.D. Damsgaard, R.E. Dunin-Borkowski, C. Hebert, J. Vanherle, and A. Hessler-Wyser: *J. Mater. Sci.*, 2013, vol. 48, pp. 2893–2907.
25. S. Deville, E. Saiz, and A.P. Tomsia: *Biomaterials*, 2006, vol. 27, pp. 5480–89.
26. K. Nagashima and Y. Furukawa: *J. Cryst. Growth*, 1997, vol. 171, pp. 577–85.
27. G.W. Young, S.H. Davis, and K. Brattkus: *J. Cryst. Growth*, 1987, vol. 83, pp. 560–71.
28. S. Deville: *Adv. Eng. Mater.*, 2008, vol. 10, pp. 155–69.
29. S. Deville, E. Saiz, and A.P. Tomsia: *Acta Mater.*, 2007, vol. 53, pp. 1965–74.
30. W.L. Li, K. Lu, and J.Y. Walz: *Int. Mater. Rev.*, 2012, vol. 57, pp. 37–60.
31. U.G.K. Wegst, M. Schecter, A.E. Donius, and P.M. Hunger: *Philos. Trans. R. Soc. London Ser. A*, 2010, vol. 368, pp. 2099–21.
32. D.H. Napper: *Polymeric Stabilization of Colloidal Dispersions*, Academic Press, London, 1983, vol. 18.
33. S. Padilla, R. Garcia-Carrodegua, and M. Vallet-Regi: *J. Eur. Ceram. Soc.*, 2004, vol. 24, pp. 2223–32.
34. S. Sanchez-Salcedo, J. Werner, and M. Vallet-Regi: *Acta Biomater.*, 2008, vol. 4, pp. 913–22.
35. W.W. Mullins and R.F. Sekerka: *J. Appl. Phys.*, 1964, vol. 35, pp. 444–51.
36. W.F. Gale and T.C. Totemeier: *Smithells Metals Reference Book*, 8th ed., Elsevier Butterworth-Heinemann, Alabama, US, 2013.
37. H. Choi, O.-H. Kim, M. Kim, H. Choe, Y.-H. Cho, Y.-H. Cho, and Y.-E. Sung: *ACS Appl. Mater. Int.*, 2014, vol. 6, pp. 7665–71.
38. K.P. Dharmasena and H.N.G. Wadley: *J. Mater. Res.*, 2002, vol. 17, pp. 625–31.
39. R.W. Revie and H.H. Uhlig: *Uhlig's Corrosion Handbook*, 3rd ed., Wiley, New Jersey, US, 2011.